Inorg. Chem. **2007**, *46*, 6329–6337

Highly Uniform and Monodisperse β-$NaYF_4$:Ln^{3+} (Ln = Eu, Tb, Yb/Er, and Yb/Tm) Hexagonal Microprism Crystals: Hydrothermal Synthesis and Luminescent Properties

Chunxia Li, Zewei Quan, Jun Yang, Piaoping Yang, and Jun Lin*

Key Laboratory of Rare Earth Chemistry and Physics, Changchun Institute of Applied Chemistry, Chinese Academy of Sciences, Changchun 130022, and Graduate University of the Chinese Academy of Sciences, Beijing 100049, PR China

Received February 21, 2007

β-$NaYF_4$:Ln^{3+} (Ln = Eu, Tb, Yb/Er, and Yb/Tm) hexagonal microprisms with remarkably uniform morphology and size have been synthesized via a facile hydrothermal route. X-ray diffraction (XRD), scanning electron microscopy (SEM), transmission electron microscopy (TEM), high-resolution transmission electron microscopy (HRTEM), and photoluminescence (PL) spectra as well as kinetic decays were used to characterize the samples. It is found that sodium citrate as a shape modifier introduced into the reaction system plays a critical role in the shape evolution of the final products. Furthermore, the shape and size of the products can be further manipulated by adjusting the molar ratio of citrate/RE^{3+} (RE represents the total amount of Y^{3+} and the doped rare earth elements such as Eu^{3+}, Tb^{3+}, Yb^{3+}/Er^{3+}, or Yb^{3+}/Tm^{3+}). Under the excitation of 397 nm ultraviolet light, $NaYF_4$:xEu^{3+} (x = 1.5, 5%) shows the emission lines of Eu^{3+} corresponding to $^5D_{0-3} \rightarrow {}^7F_J$ (J = 0–4) transitions from 400 to 700 nm (whole visible spectral region) with different intensity, resulting in yellow and red down-conversion (DC) light emissions, respectively. When doped with 5% Tb^{3+} ions, the strong DC fluorescence corresponding to $^5D_4 \rightarrow {}^7F_J$ (J = 6, 5, 4, 3) transitions with $^5D_4 \rightarrow {}^7F_5$ (green emission at 544 nm) being the most prominent group that has been observed. In addition, under 980 nm laser excitation, the Yb^{3+}/Er^{3+}- and Yb^{3+}/Tm^{3+}-codoped β-$NaYF_4$ samples exhibit bright green and whitish blue up-conversion (UC) luminescence, respectively. The luminescence mechanisms for the doped lanthanide ions were thoroughly analyzed.

1. Introduction

Controlled synthesis of well-defined inorganic crystals with uniform dimensions and shape is of extraordinary importance because the electronic structure, bonding, surface energy, and chemical reactivity are directly related to their surface morphology.[1] To date, numerous efforts have been devoted to the exploration of various convenient and efficient approaches for the fabrication of different kinds of inorganic crystals with multiple shapes, including rods, whiskers, and microboxes.[2−4] In these fabrications, the use of organic additives as the "shape modifier" is a common strategy to adjust and control the morphology and size of the products. Organic molecules are known to either promote or inhibit crystal growth through modifying crystal growth dynamically. By properly choosing organic additives that might have specific molecular complementarity with their inorganic counterparts, the growth of inorganic crystals can be rationally directed to yield products with desirable morphologies and/or hierarchical structures.[5]

Rare earth fluorides normally possess a high refractive index and low phonon energy. Furthermore, they exhibit adequate thermal and environmental stability and therefore are regarded as excellent host lattices for down-conversion (DC) and up-conversion (UC) luminescence of lanthanide ions.[6,7] The DC process is the conversion of higher-energy

* To whom correspondence should be addressed. E-mail: jlin@ciac.jl.cn (Prof. Jun Lin).

(1) Li, H.; Liu, R.; Zhao, R. X.; Zheng, Y. F.; Chen, W. X.; Xu. Z. D. *Cryst. Growth Des.* **2006**, *6*, 2795.
(2) Hu, J. Q.; Chen, Q.; Xie, Z. X.; Han, G. B.; Wang, R. H.; Ren, B.; Zhang, Y.; Yang, Z. L.; Tian, Z. Q. *Adv. Funct. Mater.* **2004**, *14*, 183.
(3) Hu, J. Q.; Li, Q.; Wong, N. B.; Lee, C. S.; Lee, S. T. *Chem. Mater.* **2002**, *14*, 1216.
(4) Zhao, F. H.; Lin, W. J.; Wu, M. M.; Xu, N. S.; Yang, X. F.; Tian, Z. R.; Su, Q. *Inorg. Chem.* **2006**, *45*, 3256.
(5) Wang, X.; Zhuang, J.; Peng, Q.; Li, Y. D. *Adv. Mater.* **2006**, *18*, 2031.

10.1021/ic070335i CCC: $37.00
Published on Web 06/30/2007

photons into lower-energy photons, which is also extensively exploited in semiconductor quantum dots and organic dyes.[8] In contrast, UC is the generation of higher-energy photons from lower-energy radiation on the basis of sequential adsorption and energy-transfer steps.[9]

Among the investigated fluorides, $NaYF_4$, as one of the most efficient DC and UC host lattices, has attracted more and more attention in the field of materials science over the past two decades.[10−23] The crystal structure of $NaYF_4$ exhibits two polymorphic forms, namely, cubic (α-) and hexagonal (β-) phases, depending on the synthesis conditions and methods. The hexagonal structure of $NaYF_4$ has three cation sites, one for rare earth ions (1a), one for both rare earth and sodium ions (1f), and the third for sodium ions (2h). Sites 1a and 1f both have C_{3h} symmetry, whereas site 2h has C_s symmetry.[15] Previous investigations have shown that hexagonal β-$NaYF_4$ is a much better host lattice than the cubic α-$NaYF_4$ for the luminescence of various optically active lanthanide ions.[24,25] For example, provided that it is activated by Yb^{3+}/Er^{3+} ion pairs, the green emission of β-$NaYF_4$ is 10 times stronger and overall (green plus red) emissions are 4.4 times greater than those for the α phase. Consequently, how to obtain the pure hexagonal phase of $NaYF_4$ is the key in successfully achieving a brighter phosphor.[24] Hydrothermal treatment as a typical solution approach has proven to be an effective and convenient process in preparing various inorganic materials with a variety of controllable morphologies and architectures. This method is also suitable for the fabrication of $NaYF_4$ inorganic luminescent materials doped with different lanthanide ions or ion pairs.[20−23] Nevertheless, to the best of our knowledge, most of the reported research was predominantly focused on the fabrication of $NaYF_4$ nanocrystals with different morphologies.[10−25] Little has been done on the manufacture of $NaYF_4$ microcrystals with uniform morphology. Inorganic microcrystals with novel morphologies are of special significance in understanding the growth behavior and potential technological applications in microelectronic devices.[26,27] There are no reports concerning the self-assembled uniform $NaYF_4$ microcrystals with tunable morphology and excellent luminescent properties via a directly facile template-free synthetic route or without the aid of other techniques hitherto. Accordingly, in this Article, we describe a template-free, nonseed, and aqueous-phase process for the synthesis of uniform β-$NaYF_4$ hexagonal microprisms with tight size control and high monodispersity via a facile and mild hydrothermal method, including Eu^{3+}- or Tb^{3+}-doped DC and Yb^{3+}/Er^{3+}- or Yb^{3+}/Tm^{3+}-codoped UC $NaYF_4$ microcrystals. In the current system, sodium citrate was introduced into the reaction system to govern the shape and size of the products.[28] The effects of the molar ratio of sodium citrate to RE^{3+} (RE represents the total amount of Y^{3+} and the doped rare earth elements such as Eu^{3+}, Tb^{3+}, Yb^{3+}/Er^{3+}, or Yb^{3+}/Tm^{3+}) and reaction time on the crystal morphology and size have been investigated in detail. On the basis of the experimental results, a possible mechanism of crystal growth has been preliminarily proposed. Furthermore, the DC and UC luminescence properties of Eu^{3+}, Tb^{3+}, Yb^{3+}/Er^{3+}, and Yb^{3+}/Tm^{3+} have been thoroughly studied in the obtained β-$NaYF_4$:Ln^{3+} hexagonal microprism crystals.

2. Experimental Section

Preparation. All of the chemicals are of analytical grade reagents purchased from Beijing Chemical Corporation and used without further purification. Rare earth chloride stock solutions of 0.2 M were prepared by dissolving the corresponding metal oxide (99.999%) in hydrochloric acid at elevated temperature. All of the doping ratios of Ln^{3+} are molar in our experiments. In a typical procedure for the preparation of $NaYF_4$:5% Tb^{3+} microcrystals, 9.5 mL YCl_3 (0.2 M) and 1 mL $TbCl_3$ (0.1 M) were added into 20 mL aqueous solution containing 2 mmol sodium citrate (0.5882 g) to form the metal−citrate complex (the molar ratio of citrate to RE^{3+} is 1:1). After vigorous stirring for 30 min, 30 mL of aqueous solution containing 25 mmol of NaF (1.05 g) was introduced into the above solution. Then, the mixing solution was transferred into a Teflon bottle held in a stainless steel autoclave, sealed, and maintained at 180 °C for 24 h. As the autoclave was cooled to room-temperature naturally, the precipitates were separated by centrifugation, washed with ethanol, and deionized water in sequence, and then dried in air at 80 °C for 12 h. $NaYF_4$:$x$$Eu^{3+}$ (x = 1.5, 5%), $NaYF_4$:17% Yb^{3+}/3% Er^{3+}, and $NaYF_4$:17% Yb^{3+}/3% Tm^{3+} samples were prepared in a manner similar to that for the $NaYF_4$:5% Tb^{3+} sample. Additionally, different molar ratios (0, 1:2, 1:1, 2:1, 4:1, 8:1, 180 °C, 24 h) of sodium citrate: RE^{3+} (RE = sum of the rare earth ions) and hydrothermal treatment times

(6) Stouwdam, J. W.; van Veggel, F. C. J. M. *Nano Lett.* **2002**, *2*, 733.
(7) Yan, R. X.; Li, Y. D. *Adv. Funct. Mater.* **2005**, *15*, 763.
(8) Feldman, C.; Justel, T.; Ronda, C. R.; Schmidt, P. J. *Adv. Funct. Mater.* **2003**, *13*, 511.
(9) Wright, J. C. *Top. Appl. Phys.* **1976**, *15*, 239.
(10) Boyer, J. C.; Vetrone, F.; Cuccia, L. A.; and Capobianco, J. A. *J. Am. Chem. Soc.* **2006**, *128*, 7444.
(11) Martin, N.; Boutinaud, P.; Mahiou, R.; Cousseins, J.; Bouderbala, M. *J. Mater. Chem.* **1999**, *9*, 125.
(12) Shalav, A.; Richards, B. S.; Trupke, T.; Krämer, K. W.; Güdel, H. U. *Appl. Phys. Lett.* **2005**, *86*, 013505.
(13) Zhang, Y. W.; Sun, X.; Si, R.; You, L. P.; Yan, C. H. *J. Am. Chem. Soc.* **2005**, *127*, 3260. Mai, H. X.; Zhang, Y. W.; Si, R.; Yan, Z. G.; Sun, L. S.; You, L. P.; Yan, C. H. *J. Am. Chem. Soc.* **2006**, *128*, 6426. Thoma, R. E.; Insley, H.; Hebert, G. M. *Inorg. Chem.* **1966**, *5*, 1222. Burns, J. H. *Inorg. Chem.* **1965**, *6*, 881. Zakaria, D.; Mahiou, R.; Avignant, D.; Zahir, M. *J. Alloys Compd.* **1997**, *257*, 65.
(14) Yi, G. S.; Chow, G. M. *Chem. Mater.* **2007**, *19*, 341.
(15) Wang, F.; Chatterjee, D. K.; Li, Z. Q.; Zhang, Y.; Fan, X. P.; Wang, M. Q. *Nanotechnology* **2006**, *17*, 5786.
(16) Wang, L. Y.; Li, Y. D. *Chem. Commun.* **2006**, 2557.
(17) Lu, H. C.; Yi, G. S.; Zhao, S. Y.; Chen, D. P.; Guo, L. H.; Cheng, J. *J. Mater. Chem.* **2004**, *14*, 1336.
(18) Li, Z. Q.; Zhang, Y. *Angew. Chem., Int. Ed.* **2006**, *45*, 7732.
(19) Yi, G. S.; Chow, G. M. *Adv. Funct. Mater.* **2006**, *16*, 2324.
(20) Wang, X.; Zhuang, J.; Peng, J.; Li, Y. D. *Inorg. Chem.* **2006**, *45*, 6661.
(21) Wang, L. Y.; Yan, R. X.; Hao, Z. Y.; Wang, L.; Zeng, J. H.; Bao, J.; Wang, X.; Peng, Q.; Li, Y. D. *Angew. Chem., Int. Ed.* **2005**, *44*, 6054.
(22) Zeng, J. H.; Su, J.; Li, Z. H.; Yan, R. X.; Li, Y. D. *Adv. Mater.* **2005**, *17*, 2119. Zeng, J. H.; Li, Z. H.; Su, J.; Wang, L. Y.; Yan, R. X.; Li, Y. D. *Nanotechnology* **2006**, *17*, 3549.
(23) Wang, L. Y.; Li, Y. D. *Nano Lett.* **2006**, *6*, 1645. Wang, L. Y.; Li, Y. D. *Chem. Mater.* **2007**, *19*, 727.
(24) Krämer, K. W.; Biner, D.; Frei, G.; Güdel, H. U.; Hehlen, M. P.; Lüthi, S. R. *Chem. Mater.* **2004**, *16*, 1244.
(25) Heer, S.; Kämpe, K.; Güdel, H. U.; Haase, M. *Adv. Mater.* **2004**, *16*, 2102.
(26) Wang, Q. Q.; Xu, G.; Han, G. R. *Cryst. Growth Des.* **2006**, *6*, 1776.
(27) Wang, Z. J.; Tao, F.; Yao, L. Z.; Cai, W. L.; Li, X. G. *J. Cryst. Growth* **2006**, *290*, 296.
(28) Tian, A.; Volgt, K.; Liu, J.; Mckenzie, B.; Mcdermott, M. J.; Rodriguez, M. R.; Konishi, H.; Xu, H. F. *Nat. Mater.* **2003**, *2*, 821.

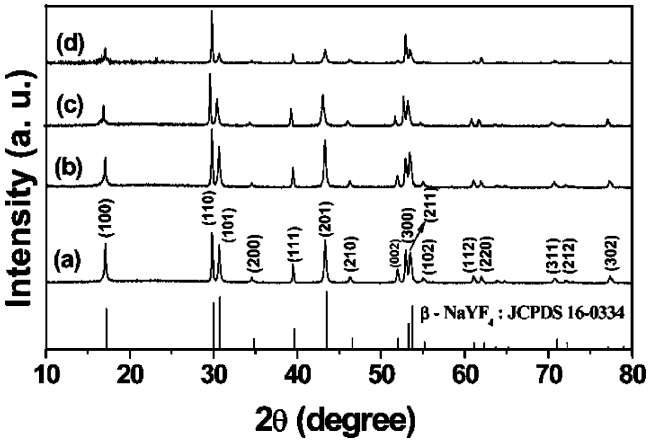

Figure 1. (a) XRD patterns for the as-prepared (a) $NaYF_4$:5% Eu^{3+}, (b) $NaYF_4$:5% Tb^{3+}, (c) $NaYF_4$:17% Yb^{3+}/3% Er^{3+}, (d) $NaYF_4$:17% Yb^{3+}/3% Tm^{3+} samples (180 °C, 24 h), and the standard data of hexagonal β-$NaYF_4$ (JCPDS no. 16−0334) as a reference.

(0.5 h, 1 h, 2 h, 7 h, 24 h, 180 °C) were selected to investigate the effects of these factors on the morphological and structural properties of the samples.

Characterizations. X-ray powder diffraction (XRD) measurements were performed on a Rigaku-Dmax 2500 diffractometer at a scanning rate of 8°/min in the 2θ range from 10 to 80°, with graphite monochromatized Cu Kα radiation (λ = 0.15405 nm). SEM micrographs were obtained using a field emission scanning electron microscope (FE-SEM, XL30, Philips). Low- to high-resolution transmission electron microscopy (TEM) was performed using a FEI Tecnai G2 S-Twin with a field emission gun operating at 200 kV. Images were acquired digitally on a Gatan multiple CCD camera. The photoluminescence (PL) excitation and emission spectra were recorded with a Hitachi F-4500 spectrophotometer equipped with a 150 W xenon lamp as the excitation source. The UC emission spectra were obtained using a 980 nm laser from an OPO (optical parametric oscillator, Continuum Surelite, USA) as the excitation source and detected by R955 (HAMAMATSU) from 400 to 900 nm. The PL lifetimes of the samples were measured with a Lecroy Wave Runner 6100 Digital Oscilloscope (1GHz) using a tunable laser (pulse width = 4 ns) as the excitation source (Continuum Sunlite OPO). All of the measurements were performed at room temperature.

3. Results and Discussion

Structure and Morphology. The composition and phase purity of the products were first examined by XRD. Figure 1 shows the XRD patterns of the as-prepared $NaYF_4$:Ln^{3+} (Ln = Eu, Tb, Yb/Er, and Yb/Tm) products. All of the four samples exhibit the peaks of pure crystalline hexagonal β-$NaYF_4$ (space group: $P6_3/m$), which are consistent with the literature data (JCPDS no. 16−0334). No second phase is detected in the XRD patterns, revealing that Eu^{3+}, Tb^{3+}, Yb^{3+}/Er^{3+}, and Yb^{3+}/Tm^{3+} have been effectively doped into the host lattices of β-$NaYF_4$ (parts a−d of Figure 1). As a result of the preferential growth effect caused by different synthesis routes, the relative intensities of (110) and (101) and (300) and (211) planes in our hydrothermal process derived β-$NaYF_4$:Ln^{3+} samples are a little different from those in JCPDS 16−0334 (solid-state reaction derived sample). Moreover, as can be seen from the XRD patterns, high crystallinity can be obtained at a relatively low

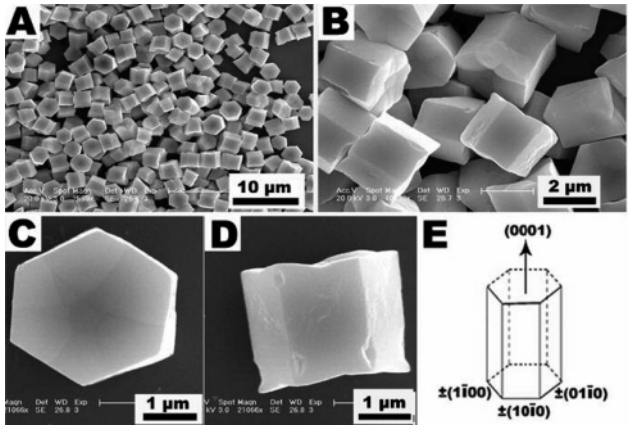

Figure 2. (A) Lower magnification, (B) higher magnification, (C, D) typical individual SEM images for the as-prepared β-$NaYF_4$:5% Tb^{3+} sample, and (E) schematic diagram showing the anisotropy of the hexagonal β-$NaYF_4$ crystal.

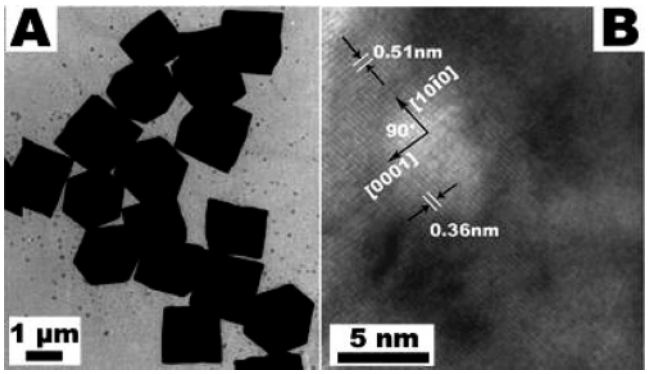

Figure 3. (A) TEM and (B) HRTEM images for the as-prepared β-$NaYF_4$: 5% Tb^{3+} sample.

hydrothermal treatment temperature (180 °C). This is important for phosphors, because high crystallinity generally means less traps and stronger luminescence.[29]

The general morphologies and the structures of the as-prepared samples are independent of the doped Ln^{3+} ions in β-$NaYF_4$. The typical SEM images for β-$NaYF_4$:5% Tb^{3+} sample are shown in Figure 2. As can be seen from a low-magnification SEM image (Figure 2A), the as-synthesized sample consists of a large quantity of hexagonal microprisms with perfect uniformity, monodispersity, and well-defined crystallographic facets. Analysis of a number of the microprisms shows that these microprisms have an average size of 3.3 μm in diameter and 1.6 μm in height. Furthermore, from the images of a higher magnification (Figure 2B) and typical individual microprisms (parts C and D of Figure 2), we can see that both the tops and bottoms of these microprisms exhibit clear strains with concave centers, whereas the side planes are relatively smoother. Figure 3 shows the typical TEM and HRTEM images of the β-$NaYF_4$: 5% Tb^{3+} sample, which provide further insight into the micrometer-scale details of the hexagonal prisms. In Figure 3A, regular hexagonal and square images can be observed, which correspond to hexagonal microprisms that are perpendicular and parallel to the copper grids, respectively.

(29) Jiang, X. C.; Sun, L. D.; Feng, W.; Yan, C. H. *Cryst. Growth Des.* **2004**, *4*, 517.

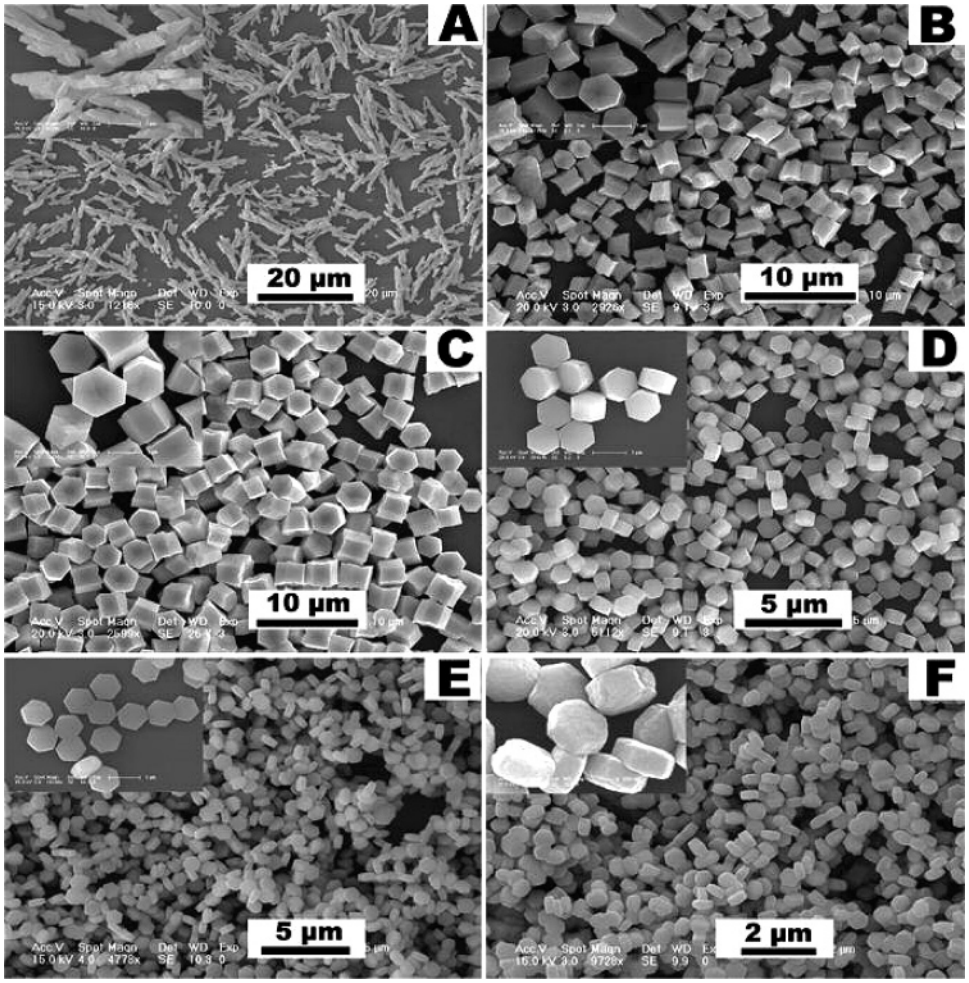

Figure 4. SEM images for β-$NaYF_4$:5% Tb^{3+} samples prepared with different molar ratios of sodium citrate:RE^{3+}. (A) 0 (without sodium citrate), (B) 1:2, (C) 1:1, (D) 2:1, (E) 4:1, (F) 8:1. All of the samples were hydrothermally treated at 180 °C for 24 h. Insets are higher-magnification images for the corresponding samples.

Typical widths and angles of the hexagon and square are about 1.6 and 1.6 μm and 120 and 90°, respectively. These values are consistent with those observed from SEM images (parts C and D of Figure 2). The corresponding HRTEM image (Figure 3B) recorded from a hexagonal cross section shows high crystallinity of the β-$NaYF_4$:5% Tb^{3+} products. It is well known that the surfaces of a hexagonal microprism are typically $\{000\bar{1}\}$ top/bottom planes and six energetically equivalent $\{10\bar{1}0\}$ families of prismatic planes, consisting of $\pm(10\bar{1}0)$, $\pm(01\bar{1}0)$, and $\pm(1\bar{1}00)$,[26,30] as shown in Figure 2E. In our case, the interplanar distances between adjacent lattice planes are determined as ~0.51 and 0.36 nm, corresponding to the d-spacing values of the $(10\bar{1}0)$ and (0001) planes, respectively.[15,25]

Effect of Sodium Citrate Content. Here, we stress the important influence of the molar ratios of sodium citrate ($Na_3C_6H_5O_7$) to RE^{3+} on the shape formation of hexagonal microprisms in our current synthesis. Table S1 (Supporting Information) lists the changes in morphology and size for the as-prepared β-$NaYF_4$:5% Tb^{3+} products with different molar ratios of sodium citrate:RE^{3+} obtained at 180 °C for 24 h. Figure 4 shows the corresponding particle sizes and morphology variation of β-$NaYF_4$:5% Tb^{3+} products. Without sodium citrate, β-$NaYF_4$ crystals tend to grow into irregular structures with an average length of 7.5 μm instead of uniform hexagonal microprism crystals, as shown in Figure 4A. The high-magnification image (inset in Figure 4A) shows that the surface of these particles is coarse. However, once sodium citrate is introduced into the reaction system, significant change takes place in morphology of crystals. Figure 4B shows the SEM images of the sample synthesized with 1:2 of sodium citrate:RE^{3+}. The images reveal that the products are hexagonal microprisms with an average diameter of 1.8 μm and a height of 2.2 μm, respectively. This indicates that the citrate anions are responsible for the morphology transition from irregular shape to hexagonal microprisms. The exact mechanism for the change of morphology of β-$NaYF_4$ grown with and without sodium citrate is not very clear. It might be explained in terms of the kinetics of the crystal growth process. In the past decade, many researches have been done on the growth mechanism of hexagonal prismatic crystals.[31−33] Leaudise

(30) Hsuch, T. J.; Chang, S. J.; Lin, Y. R.; Tsai, S. Y.; Chen, I. C.; Hsu, C. L. *Cryst. Growth Des.* **2006**, *6*, 1282.
(31) Li, W. J.; Shi, E. W.; Zhong, W. Z.; Yin, Z. W. *J. Cryst. Growth* **1998**, *203*, 186.
(32) Laudise, R. A.; Ballman, A. A. *J. Phys. Chem.* **1960**, *64*, 688.

et al.[33] claimed that the growth of crystals is related to the relative growth rate of different crystal facets and the difference in the growth rates of various crystal facets results in a different outlook of the crystallite. Stephen[34] also pointed out that the unit cell symmetry governs the spatial relations between the facets, however, their selection is mechanistically determined by the relative rates of growth along different crystallographic directions. In general, facets perpendicular to the fast directions of growth have smaller surfaces areas and slow growing faces therefore dominate the morphology. In case of the β-$NaYF_4$ hexagonal microprisms, the areas of the $\{10\bar{1}0\}$ planes exceed those of $\{0001\}$. This feature implies that these two planes have the lowest surface energy and that the surface energy of the $\{10\bar{1}0\}$ planes is much lower than that of $\{0001\}$ under the conditions used for the microprism growth. So, the velocity of different crystallographic planes descends in the order, $\nu(0001) > \nu(10\bar{1}0) > \nu(000\bar{1})$.[35] In the absence of sodium citrate, the crystals grow predominantly along the $<0001>$ direction, leading to the formation of an irregular shape with an average length up to 7.5 μm. In the presence of sodium citrate, uniform hexagonal microprisms with an average diameter of 3.3 μm are produced, and the average height of microprisms decreases remarkably to 2.2 μm. It can be concluded that sodium citrate has the function of inhibiting the longitudinal growth along the $<0001>$ orientation with a relative enhancement of the growth sideways along $<10\bar{1}0>$ directions in the form of hexagonal prisms. Such phenomenon can be compared with the fact that the growth along the $<001>$ direction was restricted by adsorbing additives such as citrate[36,37] and phosphate ions[38] on the (001) surfaces of ZnO, resulting in the formation of thin ZnO nanoplates.

Compared with the morphology prepared with 1:1 of citrate:RE^{3+}, the edges of six prismatic surfaces of the β-$NaYF_4$:5% Tb^{3+} sample prepared with 1:2 citrate:RE^{3+} are not uneven in length. This implies that the lower sodium citrate percentage does not facilitate the equilibrium and equivalent growth of different side surfaces. Furthermore, the degree of concave structures at the center of the top/bottom facets in the latter is much larger than that in the former, demonstrating that the growth rate of the prismatic planes is a little faster than that of the top/bottom planes, leading to the formation of a deeper concave center. With the increase of the citrate:RE^{3+} molar ratio up to 2:1 and 4:1, the corresponding products obtained under these conditions are still hexagonal prisms. However, all of the surfaces of the particles are much smoother, as shown in parts D and E of Figure 4, respectively. In addition, the concave central parts at the top/bottom planes disappear. When the molar ratio of citrate:RE^{3+} is equal to 8:1, there is no further change in morphology, but the surface of the particles becomes very coarse (Figure 4F). Interestingly, the dimensions of the diameter and height of the particles reduce systematically with the increase in the molar ratio of sodium citrate:RE^{3+} (Table S1). This indicates that the capping ability of sodium citrate increases significantly with the increase in its amount so that the crystal growth is completely restricted along all directions, leading to smaller and thinner β-$NaYF_4$ hexagonal prisms, as observed. Furthermore, the degree of influence of sodium citrate on the $<0001>$ orientations is much larger than that of the $<10\bar{1}0>$ ones. On the basis of the above analysis, it can be concluded that the optimal molar ratio of sodium citrate:RE^{3+} for the formation of β-$NaYF_4$ hexagonal prisms is $\sim$1:1 to 4:1.

In summation, under the present experimental conditions, sodium citrate has two major effects on adjusting the final architectures of β-$NaYF_4$. First, it can slow down the nucleation and subsequent crystal growth of $NaYF_4$ particles, which is similar to the role of EDTA in the formation $NaYF_4$:Yb^{3+}/Er^{3+} spherical nanoparticles,[39] because citrate anions can form strong complexes with Ln^{3+} ions through coordination interaction. This can be confirmed by the white precipitates produced after directly mixing the aqueous solution containing Y^{3+} and sodium citrate.[40] Second, sodium citrate has the dynamic effect of adjusting the growth rates of different facets, resulting in the formation of the anisotropic prismatic geometry for the β-$NaYF_4$ crystals. However, compared with the other previously known organic additives such as ethylenediamine (en) used in the formation of ZnS,[41,42] the effect of citrate anions on the morphologies or structures of the products is quite different. Take the formation ZnS nanosheets for example;[41] a lamellar precursor of $ZnS(en)_{0.5}$ was obtained by a solvothermal reaction of $Zn(Ac)_2 \cdot 2H_2O$ with thiourea in ethylenediamine at 180 °C for 12 h, in which ethylenediamine served not only as a solvent but also as a coordinating agent; then wurtzite ZnS nanosheets were obtained by thermal decomposition of the precursor in a vacuum at 250 °C for 0.5 h. Whereas in our case, at first, $Y^{3+}-$citrate complex was formed; then, under the hydrothermal condition (higher temperature and pressure), the chelating of the $Y^{3+}-$citrate complex would be weakened and Y^{3+} would be released gradually. However, F^- and Na^+ in the solution reacted with Y^{3+} to generate $NaYF_4$ nuclei. Then, α-$NaYF_4$ spherical particles transferred to β-$NaYF_4$ hexagonal prisms with the reaction proceeding.

Effect of Reaction Time-Formation Process. Because the crystal structure of $NaYF_4$ exhibits cubic (α-) and hexagonal (β-) two polymorphic forms, the phase transformation process was first investigated with an extended reaction time at the same hydrothermal temperature (180 °C). Figure 5 shows the XRD patterns of the $NaYF_4$: 5% Tb^{3+}

(33) Laudise, R. A.; Kolb, E. D.; Caporaso, A. J. *J. Am. Chem. Soc.* **1964**, *47*, 9.
(34) Stephen, M. *Angew. Chem., Int. Ed.* **2000**, *39*, 3392.
(35) Jang, E. S.; Won, J. H.; Hwang, S. J.; Choy, J. H. *Adv. Mater.* **2006**, *18*, 3309.
(36) Tian, Z. R.; Viogt, J. A.; Liu, J.; Meckenzie, B.; Mcdermott, M. J. *J. Am. Chem. Soc.* **2002**, *124*, 12954.
(37) Liang, J. B.; Liu, J. W.; Xie, Q.; Bai, S.; Yu, W. C.; Qian, Y. T. *J. Phys. Chem. B* **2005**, *109*, 9463.
(38) Lmai, H.; Iwai, S.; Yamabi, S. *Chem. Lett.* **2004**, *33*, 768.
(39) Yi, G. S.; Lu, H. C.; Zhao, S. Y.; Yue, G.; Wang, W. J.; Chen, D. P.; Guo, L. H. *Nano Lett.* **2004**, *4*, 2191.
(40) Huignard, A.; Buissette, V.; Laurent, G.; Gacoin, T.; Boilot, J. P. *Chem. Mater.* **2002**, *14*, 2264.
(41) Yu, S. H.; Yoshimura, M. *Adv. Mater.* **2002**, *14*, 296.
(42) Chen, X. J.; Xu, H. F.; Xu, N. S.; Zhao, F. H.; Lin, W. J.; Lin, G.; Fu, Y. L.; Huang, Z. L.; Wang, H. Z.; Wu, M. M. *Inorg. Chem.* **2003**, *42*, 3100. Deng, Z. X.; Wang, C.; Sun, X. M.; Li, Y. D. *Inorg. Chem.* **2002**, *41*, 869.

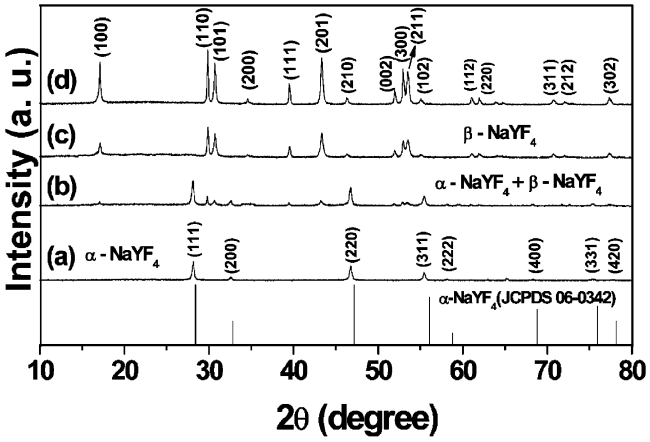

Figure 5. XRD patterns for $NaYF_4$:5% Tb^{3+} samples (molar ratio for sodium citrate:RE^{3+} = 1:1, 180 °C) as a function of reaction time. (a) 0.5 h, (b) 1 h, (c) 2 h, and (d) 24 h. The standard data of cubic α-$NaYF_4$ (JCPDS no. 06−0342) are given as a reference.

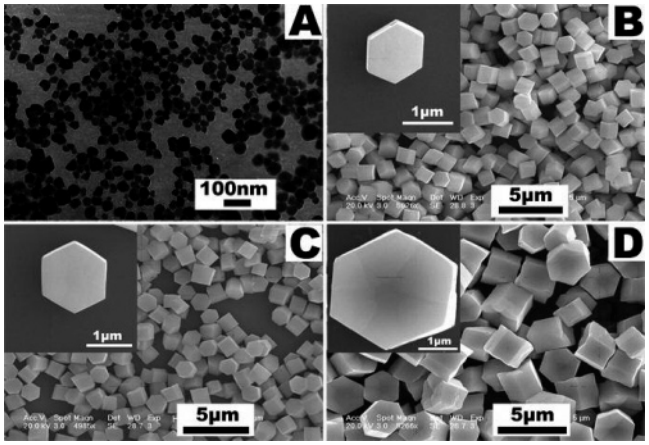

Figure 6. (A) TEM and (B−D) SEM images for $NaYF_4$:5% Tb^{3+} samples (molar ratio for sodium citrate:RE^{3+} = 1:1, 180 °C) as a function of reaction time. (A) 0.5 h, (B) 1 h, (C) 7 h, (D) 24 h.

samples prepared with 1:1 citrate/RE^{3+} at different reaction times. It reveals that the samples display distinctively different XRD patterns at different reaction times. The sample obtained at t = 0.5 h shows a unique XRD pattern (Figure 5a) due to pure cubic (α-) $NaYF_4$ phase (JCPDS no. 06−0342). When the reaction time increased to 1 h, a new β-$NaYF_4$ phase emerged in addition to the α-$NaYF_4$ phase, as shown in Figure 5b. This indicated that the samples transformed partially from α to β phase with reaction time prolongation. With the further reaction, from 1 to 2 h, the fraction of the β phase increased remarkably. As the reaction time extended to 2 h, the α phase disappeared completely and only the β phase existed (Figure 5c). The intensities of the diffraction peaks in Figure 5d (t = 24 h) increase significantly with respect to those in Figure 5d (t = 2 h), implying that the crystallinity of the sample increases with the increase of reaction time. In the previous research,[39] the α → β phase transition process of $NaYF_4$ was reported as an endothermic process. Moreover, for $NaYF_4$, the β phase is more thermodynamically stable than the α phase.[43] In our experiment, it took only 2 h to transfer completely from the α phase to the β phase. Thus, it is reasonable that the present synthetic conditions may be preferable for achieving β-$NaYF_4$, indicating that our method is facile and effective to obtain crystalline pure products of β-$NaYF_4$.

At the same time, the morphologies of the samples were carefully investigated by quenching the reaction at different time intervals. Figure 6 shows the TEM and SEM images of $NaYF_4$:5% Tb^{3+} samples obtained with 1:1 for sodium citrate:RE^{3+} at 180 °C for various reaction periods. At t = 0.5 h, a typical TEM image (Figure 6A) revealed that the α-$NaYF_4$ sample is composed of spherical particles with a mean diameter of 60 nm. With further reaction, α-phase particles convert to β-phase ones gradually. These particles would serve as seeds for the growth of β-$NaYF_4$ hexagonal microprisms. Then, the particle edge sharpening occurs concomitantly with particle growth. With the reaction proceeding only 1 h, the fairly uniform well-defined $NaYF_4$ hexagonal microprisms with an average diameter of 1.5 μm and a height of 0.75 μm (Figure 6B) are produced on a large scale with very narrow size distribution. Furthermore, the top/bottom facets and six prismatic planes are very smooth without clear strains appearing. On the basis of the above analysis, it is obvious that the α → β phase transition directly results in the dramatic change in morphology of $NaYF_4$ crystals. The reason for that should be related to the different characteristic unit cell structures for different crystallographic phases. The α-$NaYF_4$ seeds have isotropic unit cell structures, which generally induce the isotropic growth of particles and therefore spherical particles are observed. In contrast, β-$NaYF_4$ seeds have anisotropic unit cell structures, which can induce anisotropic growth along crystallographically reactive directions, resulting in the formation of hexagonal-shaped structures, as reported previously for the formation of hexagonal nanoplates of β-$NaYF_4$:Yb^{3+}/Er^{3+}.[43] After 7 h of growth, there are no further changes in morphology, but the size of the particles increases to 1.8 μm in diameter and 1.2 μm in height (Figure 6C), indicating the transversal and longitudinal growth of the single $NaYF_4$ microstructure with time. On aging for a longer period up to 24 h, the size of the as-obtained products continues to augment significantly (3.3 μm in diameter and 1.6 μm in height). In addition, the presence of both clear strains on the tops and bottoms with the concave center demonstrates that the growth rate in the <0001> direction is a little quicker than that in the <10$\bar{1}$0> orientation, as shown in Figure 6D. Scheme 1 shows the possible formation process of hexagonal β-$NaYF_4$ microprisms.

Photoluminescence Properties. Our experimental results and previous investigations have shown that hexagonal β-$NaYF_4$ is a better host lattice for the luminescence of various optically active lanthanide ions than the cubic α-$NaYF_4$.[22,23] Accordingly, we mainly focus on the luminescence properties of Eu^{3+}, Tb^{3+}, Yb^{3+}/Er^{3+}, and Yb^{3+}/Tm^{3+} in the as-formed β-$NaYF_4$ hexagonal microprism crystals, in an effort to reveal that our current hydrothermal method is an efficient process for the preparation of this kind of fluoride phosphors.

(43) Wei, Y.; Lu, F. Q.; Zhang, X. R.; Chen, D. P. *Chem. Mater.* **2006**, *18*, 5733.

Scheme 1. Schematic Illustration for the Formation Process of Hexagonal β-$NaYF_4$ Microprism Crystals

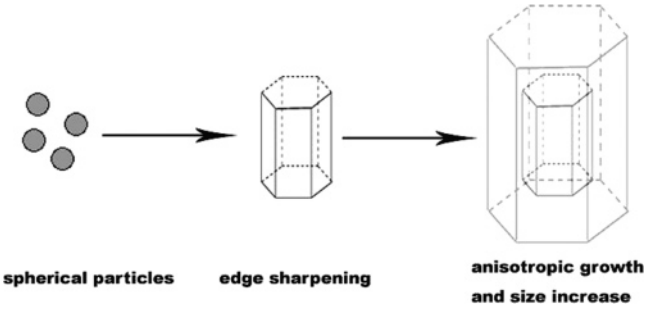

A. β-$NaYF_4$:$x$$Eu^{3+}$ (x = 1.5, 5%). Because the different doping concentrations of Eu^{3+} in host lattices greatly influence the emission intensity and the shapes of the spectra,[44] two doping concentrations of Eu^{3+} (1.5, 5%) were selected to investigate the spectral and luminescence properties in the β-$NaYF_4$:Eu^{3+} hexagonal microprism crystals. Under the excitation of longer UV light (around 400 nm), 1.5 and 5% Eu^{3+}-doped β-$NaYF_4$ samples show emissions with yellow and slightly red color, respectively. The excitation and emission spectra for the two samples are shown in parts (a)−(c) of Figure 7, respectively. Independent of the doping concentration of Eu^{3+}, the excitation spectrum (Figure 7a) consists of the characteristic excitation lines of Eu^{3+} within its $4f^6$ configuration from 200 to 550 nm, which is similar to the absorption profile for Eu^{3+} in the YF_3 host.[45] In general, most of the excitation lines can be clearly assigned (320 nm, $^7F_0 \rightarrow {}^5H_6$; 365 nm, $^7F_0 \rightarrow {}^5D_4$; 384 nm, $^7F_0 \rightarrow {}^5G_2$; 397 nm, $^7F_0 \rightarrow {}^5L_6$, strongest; 418 nm, $^7F_0 \rightarrow {}^5D_3$; 467 nm, $^7F_0 \rightarrow {}^5D_2$; 528, 537 nm, $^7F_{0,1} \rightarrow {}^5D_1$) except for those weak ones at 255, 271, 289, and 301 nm (which have little contribution to the excitation of Eu^{3+} and are of minor significance).[46] Different from the excitation spectra for Eu^{3+} in oxide hosts in which a charge-transfer band (CTB) of $Eu^{3+}-O^{2-}$ is frequently observed between 200 and 300 nm. The CTB of $Eu^{3+}-F^-$ (generally located below 200 nm) is not present in this region because of the much greater energy needed to remove an electron from F^- than from O^{2-}.[46]

Excitation into the strongest $^7F_0 \rightarrow {}^5L_6$ transition of Eu^{3+} at 397 nm yields the emission spectra of two samples, as shown in parts (b) and (c) of Figure 7, respectively. They consist of all of the emission lines associated with the Eu^{3+} transitions from the excited $^5D_{0-3}$ levels to the ^7F_J level, that is, 430 nm, $^5D_3 \rightarrow {}^7F_2$; 445 nm, $^5D_3 \rightarrow {}^7F_3$; 464 nm, $^5D_2 \rightarrow {}^7F_0$; 489 nm, $^5D_2 \rightarrow {}^7F_2$; 511 nm, $^5D_2 \rightarrow {}^7F_3$; 536 nm, $^5D_1 \rightarrow {}^7F_1$; 556 nm, $^5D_1 \rightarrow {}^7F_2$; 590 nm, $^5D_0 \rightarrow {}^7F_1$; 614 nm, $^5D_0 \rightarrow {}^7F_2$; 648 nm, $^5D_0 \rightarrow {}^7F_3$; 693 nm, $^5D_0 \rightarrow {}^7F_4$.[47] However, it is noted that the intensity ratios of I ($^5D_{1-3} \rightarrow {}^7F_J$)/I ($^5D_0 \rightarrow {}^7F_J$) in β-$NaYF_4$:5% Eu^{3+} decrease greatly with respect to those in β-$NaYF_4$:1.5% Eu^{3+}. For Eu^{3+}, whether or not the emission can occur from higher levels ($^5D_1$, $^5D_2$, $^5D_3$) together with their relative intensities depends primarily upon the doping concentration of Eu^{3+} and the dominant vibration frequencies available in the host lattice.[45] First, the presence of emissions from higher $^5D_{1-3}$ excited states can be ascribed to the lower phonon energies of the fluoride hosts.[45] The dominant phonon energy in β-$NaYF_4$ is around 360 cm^{-1},[48]

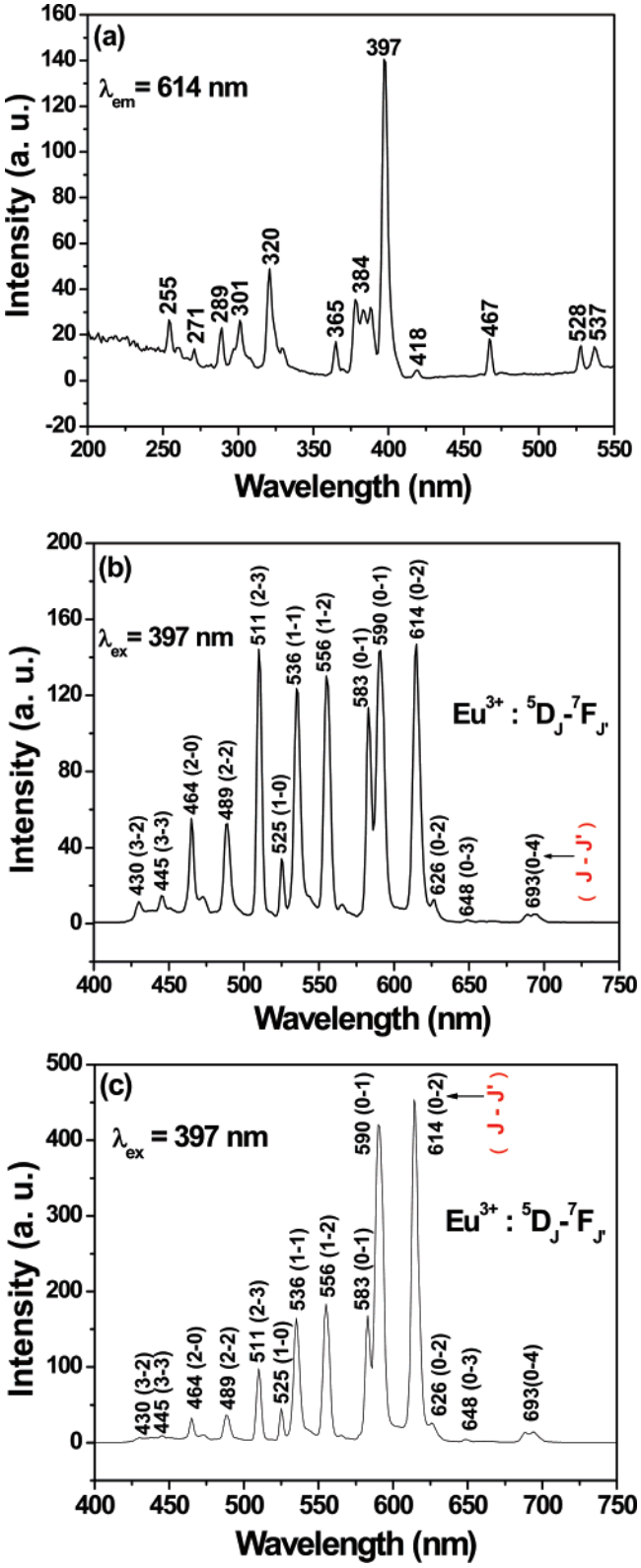

Figure 7. (a) PL excitation and (b,c) emission spectra for the (a,b) as-prepared hexagonal β-$NaYF_4$:1.5% Eu^{3+} microprism crystals and (c) β-$NaYF_4$:5% Eu^{3+} (Ex and Em slits: 2.5 nm).

(44) Stouwdam, J. W.; van Veggel, F. C. J. M. *Langmuir* **2004**, *20*, 11763.
(45) Blasse, G.; Grabmaier, B. C. *Luminescence Materials*, Springer-Verlag: Berlin, Germany, 1994.
(46) Deshazer, L. G.; Dieke, G. H. *J. Chem. Phys.* **1963**, *38*, 2190.
(47) Yu, M.; Lin, J.; Fang, J. *Chem. Mater.* **2005**, *17*, 1783.

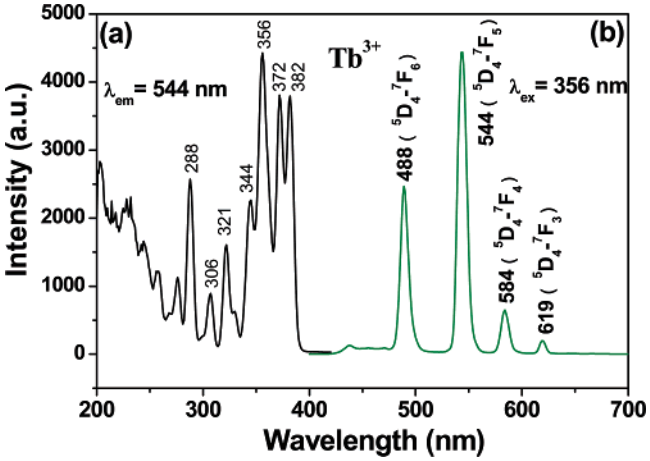

Figure 8. (a) PL excitation and (b) emission spectra for β-$NaYF_4$:5% Tb^{3+} microprism crystals (Ex and Em slits: 5.0 nm).

whereas the energy gaps for $^5D_1 \rightarrow {}^5D_0$, $^5D_2 \rightarrow {}^5D_1$, and $^5D_3 \rightarrow {}^5D_2$ of Eu^{3+} are 1751, 2563, and 2948 cm^{-1}, respectively.[45] Thus the numbers of phonons needed to bridge these neighboring excited levels are 5 ($^5D_1 \rightarrow {}^5D_0$), 7 ($^5D_2 \rightarrow {}^5D_1$), and 8 ($^5D_3 \rightarrow {}^5D_2$), respectively. It has been proposed by Blasse that the radiative rate is approximately equal to the nonradiative rate if the energy gap in the nonradiative transition amounts to 4−5 times the maximum phonon frequency of the host lattices.[49] As a result, all of the the emissions from higher-energy levels $^5D_{1-3}$ of Eu^{3+} are present, apart from the lowest $^5D_0$ excited-state in β-$NaYF_4$ host lattices (parts (b) and (c) of Figure 7). Second, although the emissions of Eu^{3+} from higher $^5D_{1-3}$ levels cannot be quenched by the multiphonon relaxations in β-$NaYF_4$, they are possibly quenched by cross relaxations, such as Eu^{3+} ($^5D_1$) + Eu^{3+} ($^7F_0$) → Eu^{3+} ($^5D_0$) + Eu^{3+}($^7F_3$) and Eu^{3+} ($^5D_3$) + Eu^{3+} ($^7F_0$) → Eu^{3+} ($^5D_2$) + Eu^{3+}($^7F_4$), which will occur only above a certain concentration of Eu^{3+} because this process depends on the interaction between two Eu^{3+} emission centers.[45,46] This can clearly account for the decrease of the intensity ratios of I ($^5D_{1-3} \rightarrow {}^7F_J$)/I ($^5D_0 \rightarrow {}^7F_J$) in β-$NaYF_4$:5% Eu^{3+} with respect to those in β-$NaYF_4$:1.5% Eu^{3+}. Finally, it is noted that the $^5D_0 \rightarrow {}^7F_1$ and $^5D_0 \rightarrow {}^7F_2$ emissions have comparable intensity in both samples, indicating that the Eu^{3+} ions occupy the 1a and 1f sites (C_{3h} symmetry with an inversion center) and 2h sites (C_s symmetry without inversion center) simultaneously in β-$NaYF_4$ host lattices.[15] From the above results and analysis, we can tune the emission color of β-$NaYF_4$:Eu^{3+} by changing the doping concentration of Eu^{3+}. For instance, β-$NaYF_4$:1.5% Eu^{3+} exhibits yellow (CIE chromaticity coordinates x = 0.3918, y = 0.4375) (point 1 in Figure 10), whereas β-$NaYF_4$:5% Eu^{3+} shows slightly red (x = 0.4030, y = 0.2958) (point 2 in Figure 10). The emission colors might be further finely tuned by finely changing the Eu^{3+} concentration, which is of great interest and this research is ongoing.

The PL decay curves for the luminescence of Eu^{3+} (from $^5D_{0-3}$ to the ground states of ^7F_J) in β-$NaYF_4$:1.5% Eu^{3+} are shown in Figure S1 (Supporting Information). These curves can be well fitted by a single-exponential function as $I(t) = I_0 \exp(-t/\tau)$ (I_0 is the initial emission intensity at t = 0, and τ is the $^1/_e$ lifetime of the emission center), and the lifetimes for $^5D_0$ (detected at 590 nm), $^5D_1$ (detected at 556 nm), $^5D_2$ (detected at 511 nm), and $^5D_3$ (detected at 445 nm) of Eu^{3+} were determined to be 5.67, 2.76, 1.10, and 0.22 ms in β-$NaYF_4$:1.5% Eu^{3+}, respectively. Note that these lifetime values of Eu^{3+} in β-$NaYF_4$ are much longer than

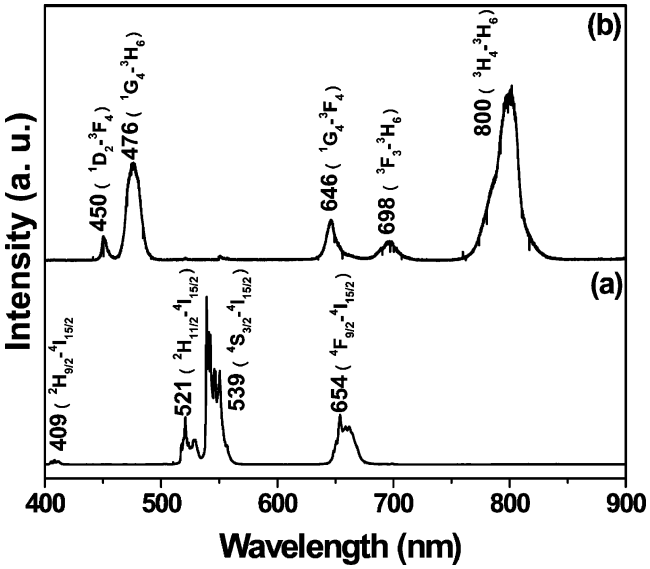

Figure 9. NIR-to-visible UC emission spectra of (a) hexagonal β-$NaYF_4$: 17% Yb^{3+}/3% Er^{3+} and (b) $NaYF_4$:17% Yb^{3+}/3% Tm^{3+} samples under 980 nm laser excitation.

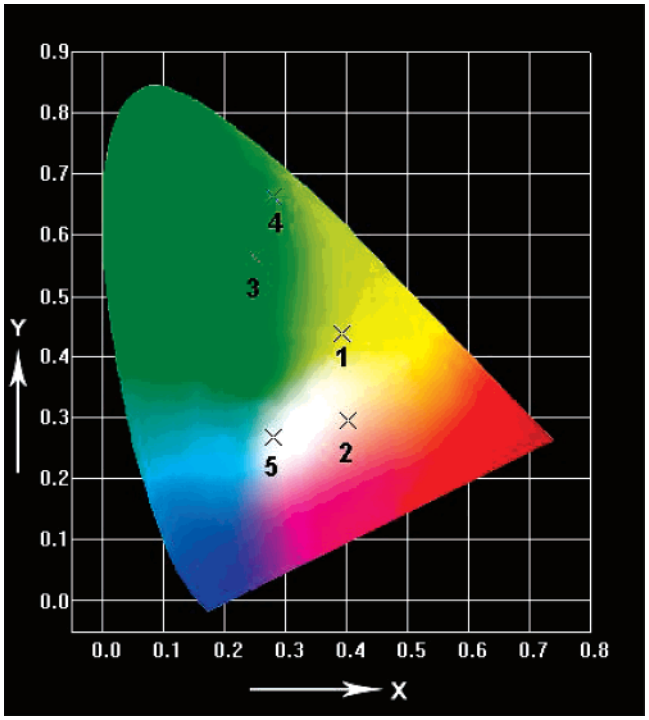

Figure 10. CIE chromaticity diagram showing the emission colors for 1.5% Eu^{3+} (**1**)-, 5% Eu^{3+} (**2**)-, 5% Tb^{3+} (**3**)-, 17% Yb^{3+}/3% Er^{3+} (**4**)-, and 17% Yb^{3+}/3% Tm^{3+} (**5**)-doped β-$NaYF_4$ micorcrystals.

(48) Suyver, J. F.; Grimm, J.; Veen, M. K. v.; Biner, D.; Krämer, K. W.; Güdel, H. U. *J. Lumin.* **2006**, *117*, 1. Diamente, P. R.; Raudsepp, M.; van Veggel, F. C. J. M. *Adv. Funct. Mater.* **2007**, *17*, 363.

(49) Blasse, G. *J. Solid State Chem.* **1988**, *18*, 79.

those (0.88 ms for $^5D_0$, 0.29 ms for $^5D_1$, 0.26 ms for $^5D_2$, and 0.14 ms for $^5D_3$) for Eu^{3+} in $CaIn_2O_4$ oxide host lattice.[50] This can also be attributed to the lower phonon frequency (360 cm^{-1}) in the former, rather than that (475 cm^{-1}) in the latter.

B. β-$NaYF_4$:Tb^{3+}. The β-$NaYF_4$:5% Tb^{3+} sample emits bright-green light under UV excitation. Figure 8 shows the excitation (a) and emission (b) spectra of the sample. The excitation spectrum (Figure 8a) is composed of the characteristic f−f transition lines within the Tb^{3+} $4f^8$ configuration. Basically, the main excitation lines can be assigned as the transitions from the $^7F_6$ ground state to the different excited states of Tb^{3+}, that is, 288 nm ($^5I_6$), 306 nm ($^5H_6$), 321 nm ($^5D_0$), 344 nm ($^5G_2$), 356 nm ($^5D_2$), 372 nm ($^5G_6$), and 382 nm ($^5D_3$), respectively.[51] Upon excitation into the $^7F_6 \rightarrow {}^5D_2$ transition at 356 nm, the obtained emission spectrum exhibits four obvious lines centered at 488, 544, 584, and 619 nm, originating from the transitions from the $^5D_4$ excited-state to the ^7F_J (J = 6, 5, 4, 3) ground states of the Tb^{3+} ion, respectively (Figure 8b), with the $^5D_4 \rightarrow {}^7F_5$ transition at 544 nm (green) as the most prominent group. The CIE coordinates for the emission spectrum of β-$NaYF_4$:5% Tb^{3+} are determined as $x = 0.2479$, $y = 0.5639$, located in the green region (point 3 in Figure 10). The lifetime for $^5D_4$ (detected at 544 nm for the $^5D_4 \rightarrow {}^7F_5$ transition) of Tb^{3+} was determined to be 0.77 ms in the β-$NaYF_4$:5% Tb^{3+} sample (Figure S2).

C. β-$NaYF_4$:Yb^{3+}/Er^{3+}, $NaYF_4$:Yb^{3+}/Tm^{3+}. A series of comparative experiments with four different doping levels of 20% Yb^{3+}/1% Er^{3+}, 20% Yb^{3+}/2% Er^{3+}, 20% Yb^{3+}/3% Er^{3+}, and 17% Yb^{3+}/3% Er^{3+} were carried out to seek the optimal doping levels of Yb^{3+}/Er^{3+}. The results indicate that the 17% Yb^{3+}/3% Er^{3+}-doped β-$NaYF_4$ microcrystals have the highest relative emission intensity under the same measurement conditions (Figure S3). So, the doping levels of 17% Yb^{3+}/3% Er^{3+} (Tm^{3+}) were chosen to investigate their UC luminescence properties. Under 980 nm IR laser excitation, the strong green and whitish blue luminescence can be observed in the 17% Yb^{3+}/3% Er^{3+} and 17% Yb^{3+}/3% Tm^{3+} ion-pair codoped β-$NaYF_4$ microcrystals, respectively. Figure 9 shows their UC spectra. These emission spectra are similar to those for Yb^{3+}/Er^{3+}- and Yb^{3+}/Tm^{3+}-activated β-$NaYF_4$ nanocrystals and bulks reported previously.[10−25] In Figure 9a for the β-$NaYF_4$:17% Yb^{3+}/3% Er^{3+} sample, the emission bands centered at 409, 521, 539, and 654 nm can be assigned to $^2H_{9/2} \rightarrow {}^4I_{15/2}$, $^2H_{11/2} \rightarrow {}^4I_{15/2}$, $^4S_{3/2} \rightarrow {}^4I_{15/2}$, and $^4F_{9/2} \rightarrow {}^4I_{15/2}$ transitions, respectively, of Er^{3+}.[17,24,48] In Figure 9b for the β-$NaYF_4$:17% Yb^{3+}/3% Tm^{3+} sample, the five emission bands centered at 450, 476, 646, and 698 nm correspond, respectively, to the $^1D_2 \rightarrow {}^3F_4$, $^1G_4 \rightarrow {}^3H_6$, $^1G_4 \rightarrow {}^3F_4$, and $^3F_3 \rightarrow {}^3H_6$ transitions of Tm^{3+}.[24,48] A strong NIR emission at 800 nm is attributed to the $^3H_4 \rightarrow {}^3H_6$ transition. The mechanisms responsible for the UC luminescence are shown in Figure S4. The CIE coordinates for the emission spectra of β-$NaYF_4$:17% Yb^{3+}/3% Er^{3+} and β-$NaYF_4$:17% Yb^{3+}/3% Tm^{3+} were determined as $x = 0.2809$, $y = 0.6631$ and $x = 0.2811$, $y = 0.2679$, respectively, as shown in points 4 and 5 in Figure 10. Furthermore, the lifetimes (fitted by a single-exponential function) for the excited states of Er^{3+}, $^2H_{11/2}$ (detected at ∼521 nm), $^4S_{3/2}$ (detected at ∼539 nm), and $^4F_{9/2}$ (detected at ∼654 nm), were found to be 53.86, 56.15, and 141.24 μs, respectively, (Figure S5), whereas those for Tm^{3+}, $^1D_2$ (detected at ∼450 nm),$^1G_4$ (detected at ∼476 nm), $^1G_4$ (detected at ∼646 nm), and $^3H_4$ (detected at ∼800 nm), were determined to be 87.42, 142.54, 163.92, and 185.00 μs, respectively, (Figure S6). Note that both Er^{3+} and Tm^{3+} show longer lifetimes in the lower excited states than those for Eu^{3+}.

4. Conclusions

We have reported a novel, efficient, environmentally benign, and solution-based one-step synthesis for lanthanide-doped β-$NaYF_4$ microcrystals with well-defined shapes and especially good uniformity. It is observed that sodium citrate acting as a shape modifier introduced into the reaction system can modulate the growth rate of different crystallographic facets to govern the formation of final morphology. Furthermore, as the molar ratio of citrate:RE^{3+} increased, the size of the hexagonal prisms decreased systematically. Under longer UV excitation, the as-prepared 1.5%, and 5% Eu^{3+}-doped β-$NaYF_4$ samples emit the yellow and red light, respectively, whereas the β-$NaYF_4$:5% Tb^{3+} sample shows a strong green emission (DC luminescence). In contrast, under 980 nm NIR laser excitation, the Yb^{3+}/Er^{3+}- and Yb^{3+}/Tm^{3+}-codoped β-$NaYF_4$ samples exhibit strong green and whitish blue UC luminescence, respectively. The DC and UC luminescence results powerfully manifest that the as-prepared β-$NaYF_4$ hexagonal microprism crystals are excellent host lattices for the luminescence of Eu^{3+} and Tb^{3+} ions and Yb^{3+}/Er^{3+} and Yb^{3+}/Tm^{3+} ion pairs. As a result of their unique luminescence properties and controlled morphology and size, these phosphors may find potential applications in the fields of color displays, light-emitting diodes (LEDs), and solid-state lasers.

Acknowledgment. This project is financially supported by the foundation of "Bairen Jihua" of Chinese Academy of Science, the MOST of China (Grant 2003CB314707), and the National Natural Science Foundation of China (Grants NSFC 50225205, 50572103, 20431030, and 00610227).

Supporting Information Available: Changes in morphology and size of β-$NaYF_4$:5% Tb^{3+} samples obtained with different molar ratios of sodium citrate/RE^{3+}, decay curves for the luminescence of Eu^{3+} and Tb^{3+}, optimum doping levels of Yb^{3+}/Er^{3+} in β-$NaYF_4$:Yb^{3+}/Er^{3+}, mechanisms responsible for the UC fluorescence of β-$NaYF_4$:Yb^{3+}/Er^{3+}(Tm^{3+}), and decay curves for the luminescence of Er^{3+} and Tm^{3+}. This material is available free of charge via the Internet at http://pubs.acs.org.

IC070335I

(50) Liu, X. M.; Lin, C. K.; Lin, J. *Appl. Phys. Lett.* **2007**, *90*, 081904.
(51) Thomas, K. S.; Singh, S.; Dieke, G. H. *J. Chem. Phys.* **1963**, *38*, 2180.